



Spin Evolution of the Magnetar SGR J1935+2154

Ming-Yu Ge¹, Yuan-Pei Yang^{2,3}, Fang-Jun Lu^{1,4}, Shi-Qi Zhou⁵, Long Ji⁵, Shuang-Nan Zhang^{1,6}, Bing Zhang^{7,8}, Liang Zhang¹,
Pei Wang⁹, Kejia Lee^{9,10}, Weiwei Zhu⁹, Jian Li^{11,12}, Xian Hou¹³, and Qiao-Chu Li^{14,15}

¹ Key Laboratory of Particle Astrophysics, Institute of High Energy Physics, Chinese Academy of Sciences, Beijing 100049, China; gemy@ihep.ac.cn

² South-Western Institute For Astronomy Research, Yunnan University, Kunming 650504, China

³ Purple Mountain Observatory, Chinese Academy of Sciences, Nanjing 210023, China

⁴ Key Laboratory of Stellar and Interstellar Physics and School of Physics and Optoelectronics, Xiangtan University, Xiangtan 411105, China

⁵ School of Physics and Astronomy, Sun Yat-Sen University, Zhuhai 519082, China

⁶ University of Chinese Academy of Sciences, Chinese Academy of Sciences, Beijing 100049, China

⁷ Nevada Center for Astrophysics, University of Nevada, Las Vegas, NV 89154, USA

⁸ Department of Physics and Astronomy, University of Nevada, Las Vegas, NV 89154, USA

⁹ National Astronomical Observatories, Chinese Academy of Sciences, Beijing 100101, China

¹⁰ Department of Astronomy, Peking University, Beijing 100871, China

¹¹ CAS Key Laboratory for Research in Galaxies and Cosmology, Department of Astronomy, University of Science and Technology of China, Hefei 230026, China

¹² School of Astronomy and Space Science, University of Science and Technology of China, Hefei 230026, China

¹³ Yunnan Observatories, Chinese Academy of Sciences, Kunming 650216, China

¹⁴ School of Astronomy and Space Science, Nanjing University, Nanjing 210023, China

¹⁵ Key laboratory of Modern Astronomy and Astrophysics, Nanjing University, Nanjing 210023, China

Received 2023 October 11; revised 2023 November 13; accepted 2023 November 16; published 2024 January 9

Abstract

Fast radio bursts (FRBs) are short pulses observed in radio frequencies usually originating from cosmological distances. The discovery of FRB 200428 and its X-ray counterpart from the Galactic magnetar SGR J1935+2154 suggests that at least some FRBs can be generated by magnetars. However, the majority of X-ray bursts from magnetars are not associated with radio emission. The fact that only in rare cases can an FRB be generated raises the question regarding the special triggering mechanism of FRBs. Here we report long time spin evolution of SGR J1935+2154 until the end of 2022. According to ν and $\dot{\nu}$, the spin evolution of SGR J1935+2154 could be divided into two stages. The first stage evolves relatively steady evolution until 2020 April 27. After the burst activity in 2020, the spin of SGR J1935+2154 shows strong variations, especially for $\dot{\nu}$. After the burst activity in 2022 October, a new spin-down glitch with $\Delta\nu/\nu = (-7.2 \pm 0.6) \times 10^{-6}$ is detected around MJD 59876, which is the second event in SGR J1935+2154. At the end, spin frequency and pulse profile do not show variations around the time of FRB 200428 and radio bursts 221014 and 221021, which supply strong clues to constrain the trigger mechanism of FRBs or radio bursts.

Key words: (stars:) pulsars: general – (stars:) pulsars: individual (SGR J1935+2154) – X-rays: bursts

1. Introduction

SGR J1935+2154 was discovered when it entered an outburst phase in 2014, which was followed by four major activity episodes in 2015 February, 2016 May to July, and 2019 November (Israel et al. 2016; Kozlova et al. 2016; Younes et al. 2017; Lin et al. 2020a, 2020b). Starting from 2020 April 27, multiple short bursts and a burst forest including hundreds of bursts from SGR J1935+2154 were detected by multiple space X-ray and Gamma-ray instruments (Younes et al. 2020b; Kaneko et al. 2021). Surprisingly, during the outburst, a double-peaked low-luminosity fast radio burst (FRB) from the direction of SGR J1935+2154 was observed by CHIME (CHIME/FRB Collaboration et al. 2020) and STARE2 (Bochenek et al. 2020) at April 28 UTC 14:34:24, which was subsequently named as FRB 200428. The fluence of FRB 200428 recorded by STARE2 (Bochenek et al. 2020) is

~ 1.5 MJy ms, making the brightness record of radio bursts from Galactic magnetars. At the same time, its X-ray counterpart, a bright X-ray burst, was detected by orbital high energy instruments such as Insight-HXMT, INTEGRAL, Konus-wind and AGILE (Mereghetti et al. 2020; Li et al. 2021; Ridnaia et al. 2021; Tavani et al. 2021). Insight-HXMT discovered the double X-ray peaks corresponding to the double radio peaks (Li et al. 2021), and both Insight-HXMT and INTEGRAL localized the X-ray burst as coming from SGR J1935+2154 (Mereghetti et al. 2020; Li et al. 2021). This is the first time that a counterpart of an FRB was detected at other wavelengths, which allowed the identification of the origin of an FRB. Two years later, SGR J1935+2154 went into a new active episode (Enoto et al. 2022; Li et al. 2022; Palm 2022; Roberts et al. 2022) at 2022 October. After the burst forest, at least two radio bursts 221014 and 221021 were captured by CHIME (Dong & Chime/Frb Collaboration 2022), GBT (Maan et al. 2022) and

Yunnan 40 m radio telescope (Huang et al. 2022) and their corresponding X-ray bursts are detected by GECAM, HEBS (GECAM-C), Konus-Wind and Insight-HXMT (Frederiks et al. 2022; Li et al. 2022; Wang et al. 2022; Younes et al. 2022).

However, the mechanism triggering FRB 200428 or FRB-like radio bursts is not well understood yet. It is widely suggested that FRBs are generated by the magnetospheric activities of magnetars, either triggered internally (Yang & Zhang 2018; Lu et al. 2020; Lyubarsky 2020; Wang et al. 2021; Yang & Zhang 2021; Li et al. 2022) or externally (Zhang 2017; Dai 2020; Zhang 2020; Geng et al. 2021). Recently, Younes et al. (2023) report that SGR J1935+2154 experienced one spin-down glitch on 2020 October 5 (MJD 59127), followed by FRB-like bursts and a pulsed radio episode (Wang et al. 2023; Zhu et al. 2023). So the timing properties of SGR J1935+2154 around the epoch of FRB events may provide crucial clues to unveil the physical process that triggered the FRB. In this work, we only focus the timing properties around FRB 200428 and burst event 221014 in 2022, considering that Younes et al. (2023) have published their results.

2. Observations and Data Analysis

2.1. Observations and Data Reduction

In this work, the observations from NICER, NuSTAR, Chandra and XMM-Newton are utilized to study the spin evolution of SGR J1935+2154 as listed in Appendix Table A1.

NICER is a payload onboard the International Space Station devoted to the study of neutron stars through soft X-ray timing (Gendreau et al. 2016). Its X-ray Timing Instrument (XTI) is an aligned collection of 56 X-ray concentrator optics (XRC) and silicon drift detector (SDD) pairs, which records individual photons with good spectral resolution and time resolution to $\sim 0.1 \mu\text{s}$ relative to the universal Time. The cleaned events data in 0.8–4.0 keV are used for profile and timing analyses by using the standard `nicerl2` command with “underonly_range=0–200”. The arrival time of each event to barycentre is corrected via `barycorr` with coordinates $\alpha = 19^{\text{h}}34^{\text{m}}55^{\text{s}}.68$ and $\delta = 21^{\circ}53'48''.2$ (Israel et al. 2016). The solar ephemeris for Solar System Barycentre (SSB) correction is DE405.

SGR J1935+2154 was observed by NuSTAR around May 02 and 11 (OBSID 80602313002, 80602313004), 2020, with corresponding exposure times of 38 and 31 ks (Harrison et al. 2013). In this work, we analyze data from two telescopes on NuSTAR (usually labeled by their focal plane modules, FPMA and FPMB) using HEASOFT (version 6.29). We utilize `nupipeline` with NuSTAR CALDB v20180312 to create GTIs and select a circular region of radius $180''$ centered on the pulsar position to extract the source spectrum. The arrival time of each photon is corrected to SSB with the same solar ephemeris.

We processed the data collected by PN of XMM-Newton from 2014 to 2020 May, (Jansen et al. 2001) using the Science Analysis System (SAS) (v14.0.01) software. The time intervals contaminated by flaring particle background are discarded. Events in a circular region with a radius of $50''$ centered on the pulsar position are selected to ensure that all the source events are included. Only PN data are utilized to perform the timing analysis considering the time resolution. The arrival time of each photon is corrected to SSB with the same solar ephemeris.

Chandra observed SGR J1935+2154 four times in 2014 and 2016, with the ObsIDs of 15874, 15875, 17314, and 18884, respectively. The corresponding time resolutions in these observations are 0.44 s, 2.85 ms, 2.85 ms, and 2.85 ms. Therefore, these four observations are used for timing analyses, as listed in Table A1. The data were reprocessed with the Chandra Interactive Analysis of Observations software (CIAO, version 4.14) using the calibration files available in the Chandra CALDB 4.9.6 database. The scientific products were extracted following the standard procedures, but adopting extraction regions with different sizes in order to properly subtract the underlying diffuse component. For 15874, we extract the events from a circular region with radius of $1''.5$ for the timing analysis. While for observations 15875, 17314 and 18884 at continuous clocking (CC) mode, events in rectangular boxes of $3'' \times 2''$ sides aligned to the CCD readout direction are used to perform timing analysis. For the timing analysis, we applied the Solar system barycentre correction to the photon arrival times with AXBARY.

2.2. Timing Analysis

We perform both partially phase-coherent timing (PPCT) analysis and fully phase-coherent timing (FPCT) analysis for SGR J1935+2154 to study its timing behaviors using TEMPO2 (Hobbs et al. 2006). The PPCT analysis can mitigate the pronounced effects of timing noise on the long term evolution and show spin evolution clearly (Ferdman et al. 2015), while the FPCT analysis can get more accurate spin parameters of the pulsar, because the timing noise such as glitches revealed by PPCT analysis can be included in the new timing model. In order to conduct PPCT analysis, it is necessary to have spin frequencies and times of arrival (ToAs) from various epochs. These data are typically acquired through Z_1^2 searching, which involves identifying the frequency that causes the folded profile to deviate the most from a uniform distribution, as indicated by the Z_1^2 value, and using it as the spin frequency for each observation. Subsequently, the phase of the minimum point in each profile is utilized as the TOA for that particular observation (Ge et al. 2012; Younes et al. 2020b).

The data used for timing analysis span in about 2300 days from MJD 56853 to 59172. Two obvious abnormalities of SGR J1935+2154 are recognised since the frequencies obtained

Table 1

The Spin Parameters of SGR J1935+2154 Obtained with Partially Phase-coherent Timing Analysis

No.	Start MJD	Finish MJD	PEPOCH MJD	ν Hz	$\dot{\nu}$ pHz s ⁻¹
1	56822	56950	56899	0.308163446(2)	-1.359(2)
2	56892	57335	57101	0.3081397240(3)	-1.35892(7)
3	56926	57605	57251	0.3081221081(3)	-1.35923(5)
4	58046	58086	58068	0.30803445(2)	-1.42(9)
5	58067	58130	58088	0.30803204(3)	-1.44(5)
6	58966	58973	58969	0.30794566(9)	0.38(1.20)
7	58970	58984	58977	0.30794430(3)	-2.99(1.32)
8	58987	59007	58996	0.30794063(3)	-3.67(18)
9	58998	59041	59017	0.307934203(8)	-3.50(3)
10	59107	59144	59126	0.307900770(6)	-3.52(2)
11	59120	59186	59149	0.30789383(1)	-3.52(2)
12	59476	59477	59476	0.307679(5)	...
13	59863	59875	59865	0.3075277(2)	-3.92(36)
14	59875	59950	59910	0.307510450(9)	-3.86(11)

with Z_1^2 searching in two epochs deviate obviously from the extrapolation of the earlier data. In order to show the spin evolution clearly, as discussed above, the PPCT analysis is performed (Ferdman et al. 2015; Ge et al. 2019), and the resulted spin parameters in different epochs are given in Table 1. The spin parameters obtained from the above mentioned time spans are then fitted with Equation (1) in TEMPO2.

$$\nu(t) = \nu_0 + \dot{\nu}_0(t - t_0) \quad (1)$$

where ν_0 , $\dot{\nu}_0$ are frequency and frequency derivative at the reference time t_0 , and t corresponds to the center of each sub-data set.

Based on the above preliminary timing results of SGR J1935+2154, we can further perform FPCT analysis to get more accurate timing solutions using the data around G1 and G2 respectively, with Equation (2) as described Lyne et al. (1992) and Ge et al. (2020).

$$\nu(t) = \begin{cases} \nu_0 + \dot{\nu}_0(t - t_0) & t < t_g \\ \nu_0 + \dot{\nu}_0(t - t_0) + \Delta\nu_p + \Delta\dot{\nu}_p(t - t_g) \\ + \Delta\nu_{d1}e^{-\frac{(t-t_g)}{\tau_{d1}}} + \Delta\nu_{d2}e^{-\frac{(t-t_g)}{\tau_{d2}}} & t \geq t_g \end{cases} \quad (2)$$

where ν_0 , $\dot{\nu}_0$ are frequency and frequency derivative at epoch t_0 , $\Delta\nu_p$ and $\Delta\dot{\nu}_p$ are the persistent offsets of frequency and frequency derivative at the glitch epoch t_g , $\Delta\nu_{d1}$, $\Delta\nu_{d2}$, τ_{d1} and τ_{d2} are the parameters of the two exponential components when $t > t_g$. The overall amplitudes of the glitches can be then inferred with $\Delta\nu = \Delta\nu_p + \Delta\nu_{d1} + \Delta\nu_{d2}$ and $\Delta\dot{\nu} = \Delta\dot{\nu}_p - \Delta\nu_{d1}/\tau_{d1} - \Delta\nu_{d2}/\tau_{d2}$. Finally, the number of the exponential

Table 2

The Timing Parameters of the Three Glitches in SGR J1935+2154

Parameters	G1	G2 ^a	G3
Epoch (MJD)	57214	58088	59865
ν (Hz)	0.3081264533(3)	0.30803203(2)	0.30752769(17)
$\dot{\nu}$ (pHz s ⁻¹)	-1.35922(4)	-1.415(19)	-3.9(4)
Glitch epoch (MJD)	57822(22)	58964.5(2.5) ^b	59876.0(5)
$\Delta\nu$ (μHz)	9.5(2)	19.8(1.4)	-2.2(2)
$\Delta\nu_p$ (μHz)	...	23.2(1.4)	...
$\Delta\dot{\nu}$ (pHz s ⁻¹)	-0.0558(0.0123)	6.3(1.1)	0.06(41)
$\Delta\dot{\nu}_p$ (pHz s ⁻¹)	...	-2.031(19)	...
$\Delta\nu_{d1}$ (μHz)	...	-5.88(9)	...
τ_{d1} (d)	...	8(1)	...
$\Delta\nu_{d2}$ (μHz)	...	2.50(16)	...
τ_{d2} (d)	...	131(6)	...
$\Delta\nu/\nu(10^{-6})$	30.8(9)	64(4)	-7.2(6)
$\Delta\dot{\nu}/\dot{\nu}$	0.041(9)	-4.4(7)	...
Time range	56822–58130	58046–59120	59864–59952
Residuals (ms)	90.9	105.6	121.1

Notes.

^a In the analyses we assume that the timing behaviors between MJD 58110 and 58965 follow the trend in MJD 58054–58110.

^b The uncertainty of the occurrence time of G2 is 2.5 days. But as discussed in the text, it definitely happened before MJD 58967.2, which is 0.4 days before FRB 200428 at MJD 58967.60857593.

components is determined by the spin behavior and the detailed timing parameters for the two glitches are listed in Table 2. The errors of spin parameters are obtained from TEMPO2 software.

For SGR J1935+2154, the timing results have not been affected by the timing accuracy of different telescopes. For NICER and NuSTAR, their time resolutions are 0.1 μs and 0.1 ms, respectively Gendreau et al. (2016); Bachetti et al. (2021), which much shorted the spin period of SGR J1935+2154. The time resolutions of XMM-Newton and Chandra observations are not as good as NICER and NuSTAR but they do not show differences on the timing results as reported in Israel et al. (2016).

3. Results**3.1. The Long-term Spin Evolution**

From the long time evolution of ν and $\dot{\nu}$ as shown in Figure 1 and Table 1, the spin behavior of SGR J1935+2154 shows strong variations, especially after the burst activity on 2020 April 27 (MJD 58966). According to the variations of ν and $\dot{\nu}$, the spin evolution of SGR J1935+2154 could be divided into two stages. The first stage is from the discovery to 2020 April 27, which shows relative steady evolution. One possible spin-up event happened according to the discontinuity of $\dot{\nu}$ and the parameters are listed in Table 2. We name this event G1 to discuss conveniently. However, G1 could not be

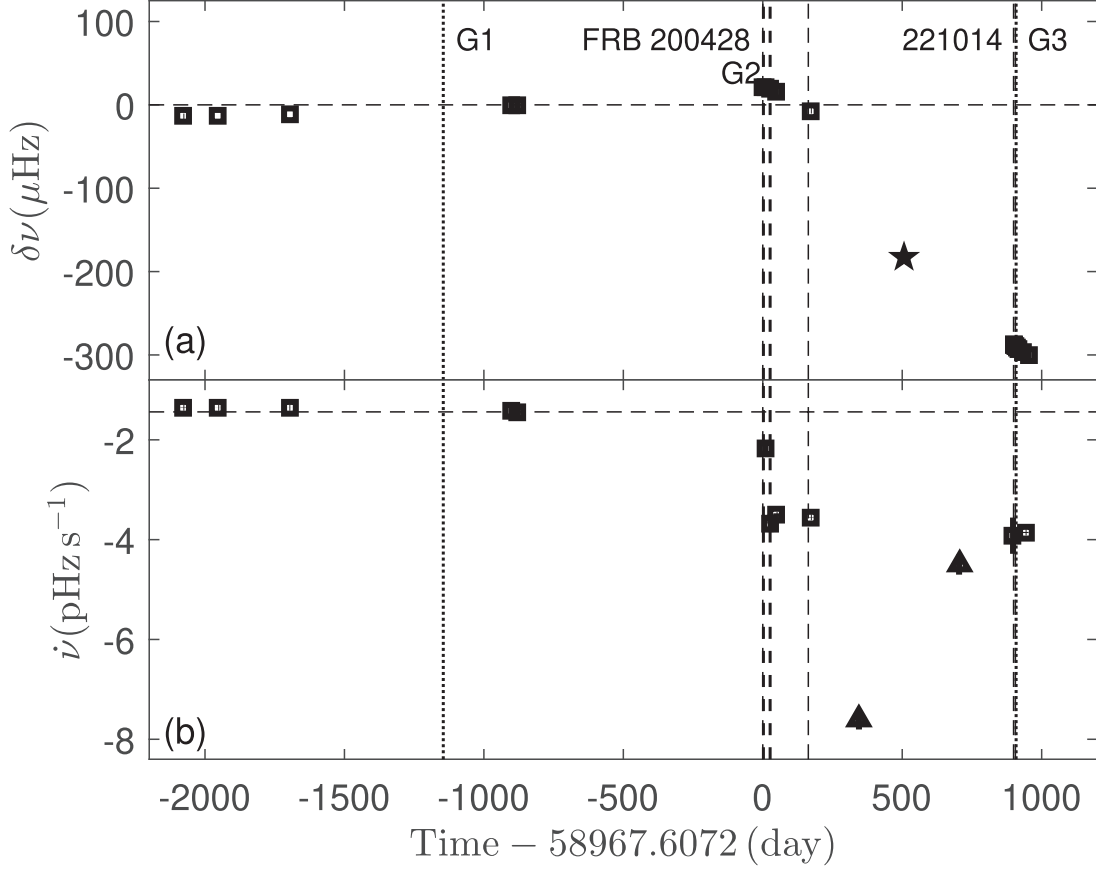


Figure 1. The whole spin evolution of SGR J1935+2154. Panel (a): The evolution of spin frequency ν by subtracting the polynomial component as parameterized in Table 1 by PPCT method. The pentagram point is obtained from NuSTAR observation 90701329002. Panel (b): The evolution of spin-down rate $\dot{\nu}$. The values of ν and $\dot{\nu}$ are obtained according to PPCT analysis and listed in Table 1. The two triangle points are estimated from NuSTAR observation 90701329002 and the adjacent spin frequencies. The vertical dashed lines represent the occurrence times of FRB 200428 and the rest radio bursts (Bochenek et al. 2020; CHIME/FRB Collaboration et al. 2020; Dong & Chime/Frb Collaboration 2022; Frederiks et al. 2022; Huang et al. 2022; Li et al. 2022; Maan et al. 2022; Wang et al. 2022). The confidence level for all the data points are 1σ level in this paper.

confirmed due to the long time gap and possible variations of spin evolution as magnetar usually do (Dib & Kaspi 2014). The second stage of the spin evolution is after the burst activity on 2020 April 27, which shows strong variations, especially for $\dot{\nu}$. The value of spin-down rate $\dot{\nu}$ increases significantly from $1.4 \times 10^{-12} \text{ Hz s}^{-1}$ to $3.5 \times 10^{-12} \text{ Hz s}^{-1}$. One spin-down glitch around MJD 59127 happened as reported in the work of Younes et al. (2023), which might trigger the radio activity. After that, the value of $\dot{\nu}$ shows large jump of $3.5 \times 10^{-12} \text{ Hz s}^{-1}$ to $7.6 \times 10^{-12} \text{ Hz s}^{-1}$ and then decreases to $4.6 \times 10^{-12} \text{ Hz s}^{-1}$ between MJD 59150 and 59860, which is comparable to the variation of 1E 1048.1-5937, PSR J1119-6127 and Swift J1818.01607 (Dib & Kaspi 2014; Dai et al. 2018; Archibald et al. 2020; Huang et al. 2021). Finally, SGR J1935+2154 experiences new strong X-ray burst activity and spin-down glitch around MJD 59876, which will be discussed in Section 3.3. In this time interval, $\dot{\nu}$ is around $-3.92 \times 10^{-12} \text{ Hz s}^{-1}$.

3.2. Spin Evolution Around FRB 200428

As shown in Figures 1 and 2(a), there is some evidence for spin discontinuity around MJD 58966 with assumption that the spin follows the evolution around MJD 58046–58130 and also discussed in the following section. Similarly, this event is named G2 to discuss conveniently. With FPCT analysis, the fitting parameters as listed in Table 2 show that G2 is frequency jump happened on MJD 58964.5(2.5) with $\Delta\nu/\nu = (6.4 \pm 0.4) \times 10^{-5}$ and $\Delta\dot{\nu}/\dot{\nu} = -4.4 \pm 0.7$, where both $\Delta\nu$ and $\Delta\dot{\nu}$ include similar delayed spin-up component. The first exponential component with $\tau_{d1} = 8 \pm 1$ day represents the delayed spin-up process that was previously detected in large glitches of the Crab pulsar and magnetar 1E 2259+586 (Woods et al. 2004; Ge et al. 2020). The second component is a slow recovery process with $\tau_{d2} = 131 \pm 6$ day and $\Delta\nu_{d2} = 2.50 \pm 0.16 \mu\text{Hz}$. Remarkably, in the evolution of the spin-down rate, a large persistent offset ($\Delta\dot{\nu}_p$) of

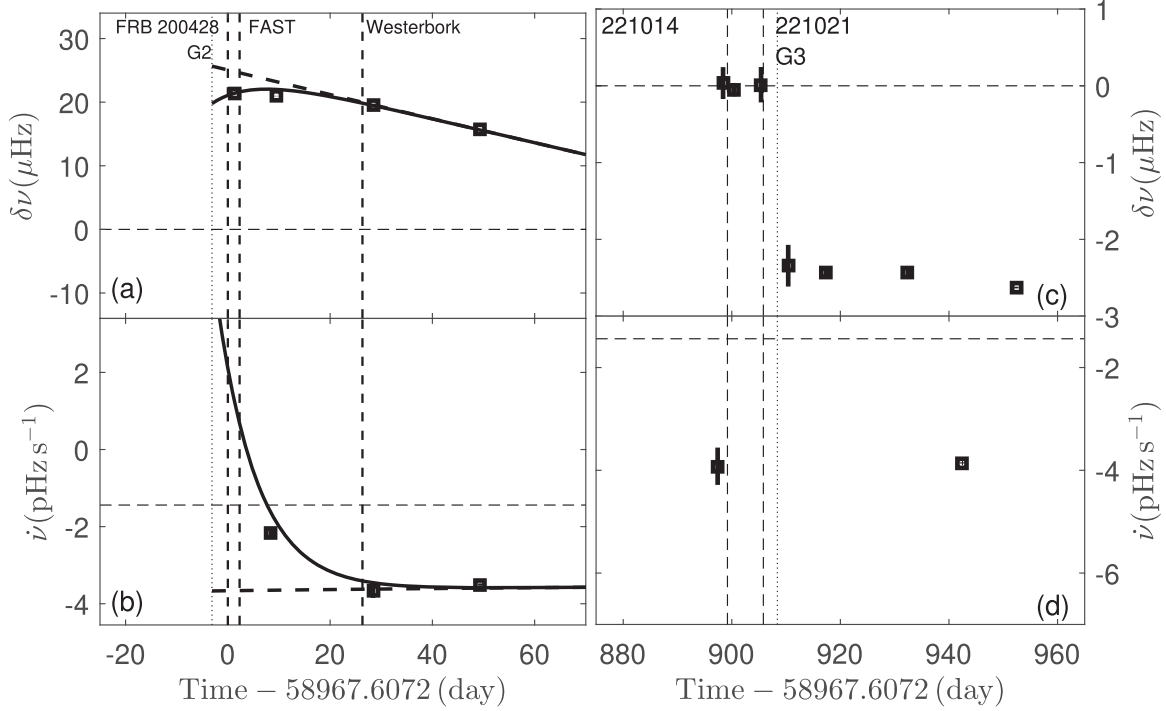


Figure 2. The spin evolution of SGR J1935+2154 after the bust activities in 2020 and 2022. Panel (a): The zoomed-in evolution of spin frequency ν around FRB 200428 as plotted in Figure 1(a). Panel (b): The zoomed-in evolution of spin-down rate $\dot{\nu}$ around FRB 200428 as plotted in Figure 1(b). The solid and dashed lines represent the fitted spin evolution including and not including the delayed spin-up components. The vertical dotted-dashed line represents the epoch of FRB 200428 while the vertical thin dotted lines represent the start epochs of burst in 2020. The two vertical dashed lines represent the occurrence time of the two weak radio bursts detected by FAST and Westerbork (Zhang et al. 2020; Kirsten et al. 2021), respectively. The dotted line represents the epoch of possible spin-up glitch at MJD 58964.5. Panels (c) and (d) are similar to (a) and (b) but for 2022. The $\delta\nu$ is subtracted with trending between MJD 59866 and MJD 59876. The vertical dashed line represents the epoch of radio bursts 221014 and 221021 (Dong & Chime/Frb Collaboration 2022; Frederiks et al. 2022; Huang et al. 2022; Li et al. 2022; Maan et al. 2022; Wang et al. 2022; Younes et al. 2022). The vertical dotted line represents the epoch of spin-down glitch at MJD 59876.

$-2.031 \pm 0.019 \text{ pHz s}^{-1}$ is present, which is 1.4 times of the spin-down rate $\dot{\nu}$ around MJD 58046–58130 and is about one order of magnitude larger than the slow recovery component. Such a persistent offset should be due to an increase in the external torque caused by a rearrangement of the magnetosphere (Link et al. 1992; Zhang et al. 2022), and the large value implies that the magnetosphere changes dramatically at the glitch, consistent with the large pulse profile changes after G2 (Younes et al. 2020b) (Figure 3).

The overall timing analyses have not given a very tight constraint on the occurrence time of G2. We therefore discuss whether it happened before FRB 200428 or not with detailed studies on timing behaviors and profiles, since it is crucial for understanding the possible causal connection between the glitch and FRB 200428. The data are divided into two parts according to the epoch of FRB 200428 as plotted in Figure 4. In Figure 5, we present the Z_1^2 variations with spin frequency for the pre-FRB data, the post-FRB data, and the entire data set. The Z_1^2 values for all three data sets reach their respective maxima at a frequency of approximately 0.3079468(12) Hz.

Notably, the Z_1^2 value for the entire data set is the highest, consistent with the findings of Younes et al. (2020b) and Borghese et al. (2020). The difference of peak frequencies is smaller than $1.2 \mu\text{Hz}$, much smaller than $19 \mu\text{Hz}$, the frequency jump of G2, meaning that G2 must happened in advance, i.e., before FRB 200428. We also fold the pre- and post-FRB pulse profiles of this magnetar with the same set of spin parameters obtained above. As shown in Figure 5, the two profiles are not different from each other significantly and share the same minimum phase, supporting the previous conclusion from another aspect. Therefore, G2 happened at least before MJD 58967.2, which is 0.4 day before FRB 200428. From these two aspects, G2 occurred at least 0.4 days before FRB 200428 and probably occurred at 3.1 ± 2.5 day earlier than FRB 200428.

We compare the delayed spin-up component of G2 with that of the glitches in the Crab pulsar and 1E 2259+586, as presented in Figure 6. Interestingly, in the $\Delta\nu/\nu-\tau_{\text{d1}}$ diagram, where τ_{d1} is the timescale of the spin-up component, all the spin-up events can be roughly fitted with a power-law function ($\alpha = 2.0$). This indicates that the mechanisms for angular momentum transfer of the glitches in the Crab pulsar, 1E 2259

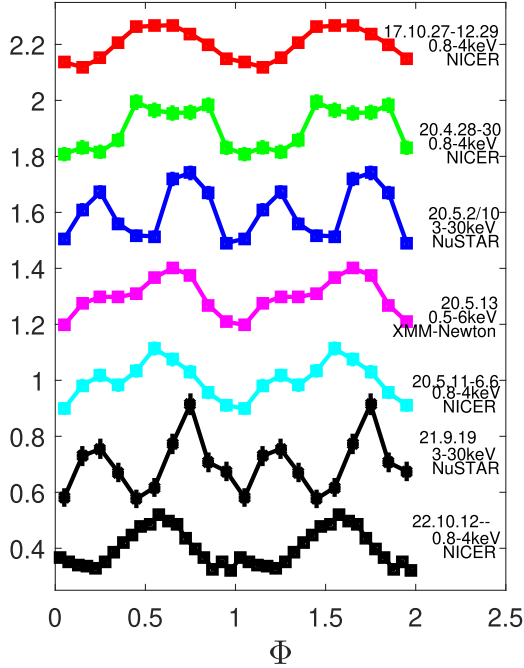


Figure 3. The X-ray pulse profiles of SGR J1935+2154 normalized by the mean count rate in different epoches. The red squares and line represent the pulse profile between MJD 58053 and 58110 (2017.10.27-29) obtained with NICER. The green squares and line represent the pulse profile obtained with NICER between MJD 58967 and 58970 (2020.04.28-05.01), which covers FRB 200428 (Borghese et al. 2020). The blue squares and line represent the pulse profile obtained with NuSTAR at MJD 58971 and 58979 (2020.05.02 and 05.10) (Borghese et al. 2020, 2022). The magenta squares and line are the pulse profile obtained with XMM-Newton at MJD 58972 (2020.05.03) (Borghese et al. 2022). The cyan squares and line represent the pulse profile between MJD 58986 and 59010 (2020.05.17-06.10) obtained with NICER. The black stars represent the pulse profile between MJD 59476 (2021.9.19) obtained with NuSTAR. The black squares and line represent the pulse profile between MJD 59863 and 59950 (2022.10.14-2023.1.8) obtained with NICER. The pulse profiles are moved upward with a step size of 0.3 to show them more clearly.

+586 and SGR J1935+2154 are similar. The existence of the rather long timescale spin-up components in the Crab pulsar and the non-detection of such components from the Vela pulsar and PSR J0537-6910 are suggested to be due to the different states of their crusts and interiors (Ge et al. 2020), i.e., the Crab pulsar is younger and hence less solidified. The existence of the delayed spin-up component of SGR J1935+2154 thus implies that it is young. It is worth noting here that the delayed spin-up components may have been detected from several other magnetars even though their timing properties are not well resolved (Woods et al. 2004; Dib & Kaspi 2014).

3.3. Spin Evolution Around Radio Burst 221014 and 221021

The spin evolution after the new burst episode 2022 October 12 is shown in Figures 2(c) and (d). A new spin-down glitch

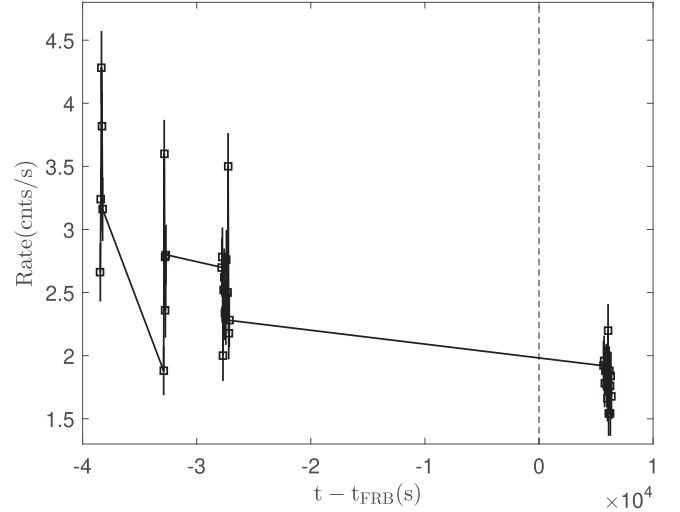


Figure 4. The lightcurve of NICER ObsID 3020560101. The light curve of burst forest is removed. The dashed line represents the time of FRB 200428.

G3 is detected around MJD 59876.0(5). As listed in Table 2, the amplitude $\Delta\nu/\nu$ of G3 is $-7.2(6) \times 10^{-6}$, which has similar amplitude of the spin-down event at MJD 59127 (Younes et al. 2023). At the same time, $\dot{\nu}$ does not change considering the measurement error, which is also similar to the spin-down event at MJD 59127 (Younes et al. 2023). Finally, we performed a PPCT analysis to investigate the presence of the exponential decay component of G3. However, our findings did not provide any evidence supporting the existence of the exponential decay component as shown in Figure 2(c).

As shown in Figures 2(c) and (d), we check the spin evolution around radio bursts 221014 and 221021 using the same method with FRB 200428. The spin evolution of SGR J1935+2154 is also steady around the time of the radio bursts 221021 and 221021, which is consistent with FRB 200428. The pulse profiles are consistent pre and post radio burst 221014 as shown in Figure 7. According to these results, the spin frequency and pulse profiles do not show variations around radio bursts 221014 and 221021. In this context, we do not present the relative phases of radio bursts 221014 and 221021 due to the unavailability of its exact arrival time (Dong & Chime/Frb Collaboration 2022; Huang et al. 2022; Maan et al. 2022).

4. Discussion

The spin evolution of magnetars is complicated from the monitoring results of RXTE, especially for 1E 1048.1-5937 (Dib et al. 2009; Dib & Kaspi 2014; Archibald et al. 2020). Due to the possible peculiar evolution of spin frequency, the phase coherent timing analysis of SGR J1935+2154 is very difficult considering the long time observation gap between MJD 58130 and MJD 58966 for G2. However, from the long

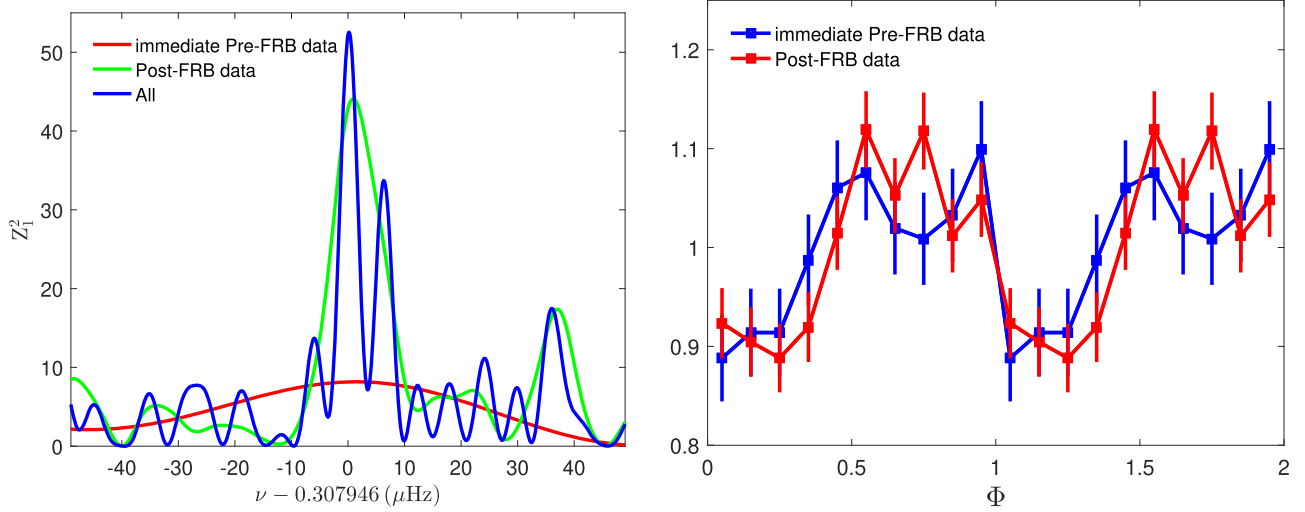


Figure 5. Z_1^2 variation with rotation frequency of SGR J1935+2154 and pulse profiles around FRB 200428 using the NICER data. Left panel: The red, green and blue lines represent the Z_1^2 values vs. frequency for the pre-FRB data (35,000–40,000 s ahead of ObsID 3020560101 as shown in Figure 4), the post-FRB data (5500–7000 s of ObsID 3020560101 and ObsIDs 3020560102, 3020560103, 3655010101 and 3655010102) and the whole data set. The curves show that the frequency remains quite stable in this duration. Right panel: The pulse profiles of SGR J1935+2154 obtained with the NICER data before and after FRB 200428. The blue points represent the pulse profile before FRB 200428, and the red points represent the pulse profile after FRB 200428.

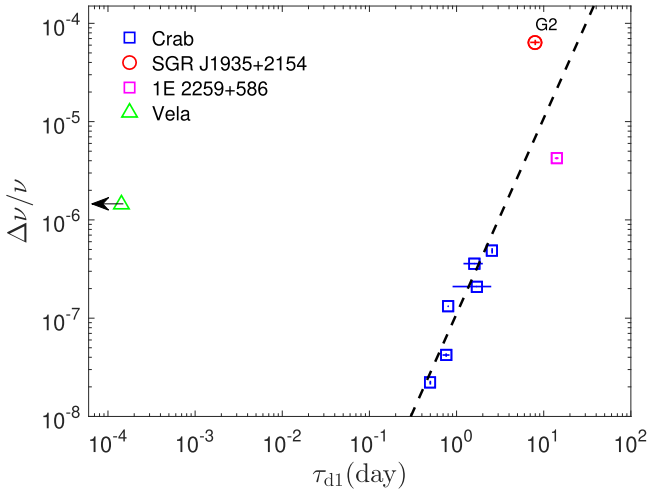


Figure 6. The correlation between $\Delta\nu/\nu$ and timescale τ_{d1} of the delayed spin-up components of glitches in the Crab pulsar, SGR J1935+2154 and 1E 2259+586. The blue squares, red circle and magenta square represent those of the Crab pulsar, SGR J1935+2154 and 1E 2259+586 (Woods et al. 2004; Ge et al. 2020; Shaw et al. 2021), respectively. The green triangle denotes the detected duration upper limit (12.4 s) of the spin frequency jump for glitches of the Vela pulsar (Palfreyman et al. 2018), which is the first for more constraint on the rise time of glitch. The dashed line represents a power-law fit with $\alpha = 2.0$.

term evolution of SGR J1935+2154 as shown in Figure 1, the variation amplitude of $\dot{\nu}$ from MJD 56822 to 58130 is smaller than the variations after MJD 58966 and also significantly smaller compared to 1E 1048.1-5937 before burst activity. As rest magnetars listed in Dib & Kaspi (2014), Dai et al. (2018), Lower et al. (2023) and Livingstone et al. (2010), the variation

amplitude of $\dot{\nu}$ before glitch and burst activity is also small. From these samples, the phase coherent timing analysis of SGR J1935+2154 before MJD 58966 is possible and the glitch behavior is reliable. However, we still could not rule out the glitch events in this time range. In the future, the observations of high cadence monitoring is encouraged using high sensitivity telescope, especially for quiescent time.

As shown in Figure 8, 1E 2259+586, 4U 0142+61, 1E 1841-045, SGR J1935+2154, PSR J1846-0258, SGR J1900+14 and PSR J1119-6127 experience ten spin-down glitch events until now (Woods et al. 1999; Livingstone et al. 2010; Gavril et al. 2011; Icdem et al. 2012; Archibald et al. 2013; Sasmaz Mus et al. 2014; Dib & Kaspi 2014; Archibald et al. 2016, 2017; Dai et al. 2018; Younes et al. 2020a, 2023). The $|\Delta\nu/\nu|$ varies from 10^{-8} to 2×10^{-4} . As indicated by Younes et al. (2023) and our research, the $|\Delta\nu/\nu|$ ratio of SGR J1935+2154 is approximately 6×10^{-6} between the two measurements, and no exponential components are observed following the glitch. This behavior is similar to SGR J1900+14 and 1E 2259+586, and differs from 4U 0142+61, PSR J1846-0258, and PSR J1119-6127, which exhibit strong exponential components (Dib & Kaspi 2014; Archibald et al. 2016, 2017; Dai et al. 2018). The potential mechanisms behind the spin-down glitch of SGR J1935+2154 are explored in studies by Tong (2023), Wu et al. (2023), and Shen et al. (2023). However, more detailed observations of SGR J1935+2154 are necessary to show the spin and emission behaviors only around anti-glitch in future.

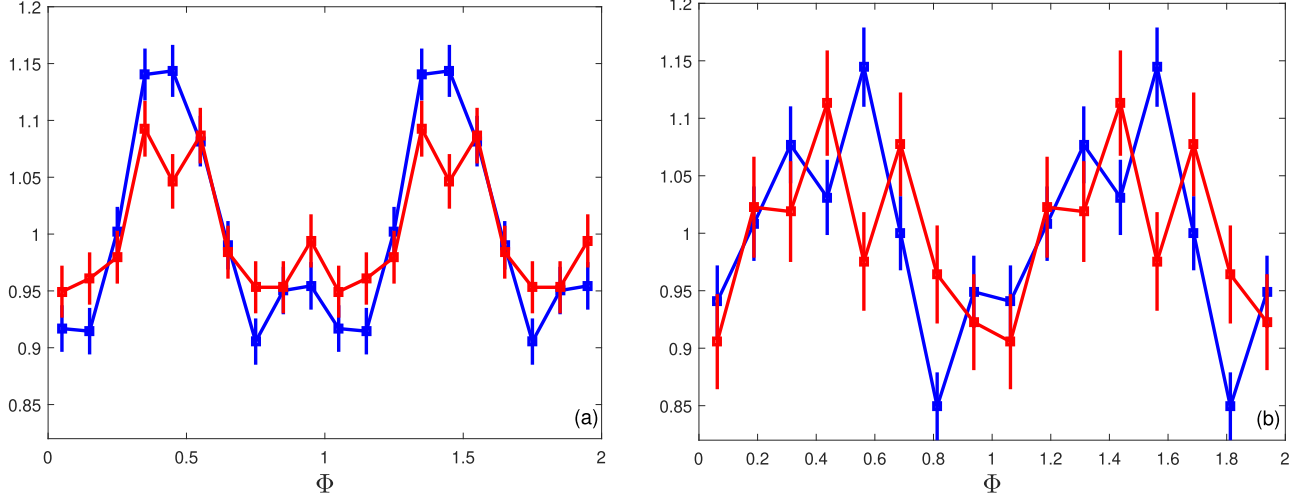


Figure 7. Pulse profiles around radio bursts 221014 and 221021. Panel (a): The pulse profiles before and after radio burst 221014. Panel (b): The pulse profiles before and after radio burst 221021. The blue and red points represent the pulse profiles before the radio bursts obtained from the NICER data in both panels, respectively.

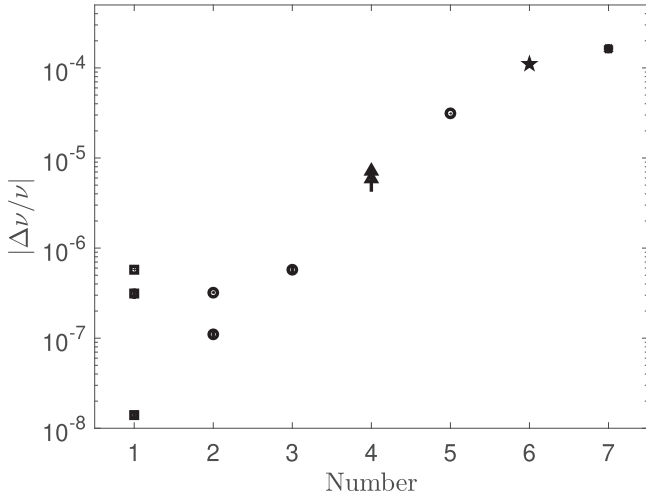


Figure 8. The spin-down glitch sample in magnetars. The numbers 1–7 represent $\Delta\nu/\nu$ of 1E 2259+586, 4U 0142+61, 1E 1841-045, SGR J1935+2154, PSR J1846-0258, SGR J1900+14 and PSR J1119-6127 (Woods et al. 1999; Livingstone et al. 2010; Gavril et al. 2011; Icdem et al. 2012; Archibald et al. 2013; Sasmaz Mus et al. 2014; Dib & Kaspi 2014; Archibald et al. 2016, 2017; Dai et al. 2018; Younes et al. 2020a, 2023).

For the physical connection between FRBs and glitches, we suggest the following scenario based on the previous theoretical framework and the observational properties of SGR J1935+2154 around the glitch. After the glitch, the motion of the core superfluid neutron vortices in the direction perpendicular to the spin axis during the spin-down relaxation phase of the glitch would alter the core magnetic field, which would result in the movement of the neutron star crust and the change in the surface magnetic field (Ruderman et al. 1998). Crustquakes are expected if the solid crust does not plastically adjust to the less-oblate equilibrium shape required by the

pulsar’s spin-down or if the magnetic stress exceeds the shear modulus (Baym & Pines 1971; Thompson & Duncan 1995; Perna & Pons 2011; Li et al. 2022). Crustal fracturing produces Alfvén waves and then generates X-ray bursts (Thompson & Duncan 1995). On the other hand, some FRB emission models proposed that FRBs are associated with magnetar activity, such as FRBs produced in the charge starvation region triggered by Alfvén waves or crust plate motions (Kumar & Bošnjak 2020; Lu et al. 2020; Wadiasingh et al. 2020; Yang & Zhang 2021), FRBs produced by relativistic plasmoids/outflows launched by Alfvén waves (Metzger et al. 2019; Yuan et al. 2020), FRBs generated by magnetic reconnection near the light-cylinder (Lyubarsky 2020), etc. Immediately after the glitch, frequent magnetic activities generate plenty of energetic charged particles in the form of electron-positron pairs, which easily power X-ray bursts. However, if FRBs are produced in the magnetosphere as proposed by some models (e.g., Kumar & Bošnjak 2020; Lu et al. 2020; Wadiasingh et al. 2020; Yang & Zhang 2021), they would be difficult to be generated in such a pair-rich environment due to the following two reasons: (1) the abundant pairs would shield the charge starvation region necessary for FRB generation; (2) even if an FRB is generated under some specific conditions, it is difficult to escape from a pair-rich magnetosphere due to a large scattering optical depth in the magnetosphere. Some time later, the magnetic field configuration becomes less irregular, as represented by the decrease of X-ray burst frequency (Cai et al. 2022). Particles can escape easily from the magnetosphere in the form of a pulsar wind like that in PSR B0540–69 after a spin-down rate transition (Ge et al. 2019). FRBs and weak radio bursts may be then generated due to the formation of the charge starvation region in the magnetosphere. This explains why FRB 200428 occurred a few days after G2 (Zhang et al. 2020; Kirsten et al. 2021).

Long after the glitch, as the crust plate is recovered and magnetic field rearrangement is finished, magnetic activities become less frequent and FRBs become more difficult to be generated. In short, FRBs preferably occur some time after the most active episodes triggered by giant glitches in magnetars. It is therefore essential to closely monitor the spin evolution of magnetars in X-rays and coordinate radio follow-up observations when a major glitch is detected in order to further test this FRB generation scenario.

5. Summary

We analyze data from NICER, NuSTAR, Chandra, and XMM-Newton to investigate the timing characteristics of SGR J1935+2154 and explore the potential trigger mechanism of FRB 200428. Based on the spin frequency ν and its derivative $\dot{\nu}$, the spin evolution of SGR J1935+2154 can be categorized into two stages. The initial stage exhibits relatively steady evolution with a $\dot{\nu} = -1.4 \times 10^{-12} \text{ Hz s}^{-1}$ prior to the burst activity in 2020 April. After the burst activity in 2020, the spin of SGR J1935+2154 shows strong variations, especially for $\dot{\nu}$. After the burst activity in 2022 October, a new spin-down glitch with $\Delta\nu/\nu = (-7.2 \pm 0.6) \times 10^{-6}$ is detected around MJD 59876, which is the second event in SGR J1935+2154. At the end, no variations of spin frequency and pulse profiles are detected around the time of FRB 200428 and radio bursts 221014 and 221021, which supply strong clues to constrain the trigger mechanism of FRB or radio bursts.

Acknowledgments

This work is supported by the National Key R&D Program of China (2021YFA0718500) from the Minister of Science and Technology of China (MOST). The authors thank supports from the National Natural Science Foundation of China under grants 12173103, 12003028, U2038101, U2038102 and 11733009. This work is also supported by International Partnership Program of Chinese Academy of Sciences (grant No. 113111KYSB20190020), the National SKA Program of China (2022SKA0130100), and the China Manned Spaced Project (CMS-CSST-2021-B11).

Appendix

Table A1
The Observation Catalog of SGR J1935+2154

Telescope	ObsID	MJD	Exposure ks
Chandra	15874	56853	10
Chandra	15875	56866	75
Chandra	17314	56900	29
Chandra	18884	57576	20
XMM-Newton	0722412501	56926	22
XMM-Newton	0722412601	56928	23

Table A1
(Continued)

Telescope	ObsID	MJD	Exposure ks
XMM-Newton	0722412701	56934	22
XMM-Newton	0722412801	56945	23
XMM-Newton	0722412901	56954	10
XMM-Newton	0722413001	56957	17
XMM-Newton	0748390801	56976	22
XMM-Newton	0764820101	57106	46
XMM-Newton	0764820201	57302	68
XMM-Newton	0871190201	58982	51
NuSTAR	80602313002	58971	37
NuSTAR	80602313004	58979	38
NuSTAR	90701329002	59476	47
NICER	1020560101	58053	3.0
NICER	1020560102	58054	13.9
NICER	1020560103	58055	8.1
NICER	1020560104	58056	5.8
NICER	1020560105	58057	0.4
NICER	1020560106	58058	2.3
NICER	1020560107	58079	1.9
NICER	1020560108	58080	6.4
NICER	1020560109	58081	2.7
NICER	1020560110	58082	5.3
NICER	1020560111	58084	2.9
NICER	1020560112	58087	1.7
NICER	1020560113	58088	0.8
NICER	1020560115	58115	0.9
NICER	1020560116	58116	0.7
NICER	2020560101	58763	0.3
NICER	2020560102	58764	2.2
NICER	2020560103	58765	2.3
NICER	2020560104	58794	1.7
NICER	3020560101	58967	3.1
NICER	3020560102	58968	0.9
NICER	3655010101	58968	0.8
NICER	3655010102	58969	3.9
NICER	3020560103	58969	0.7
NICER	3020560104	58980	0.9
NICER	3655010201	58987	4.7
NICER	3020560105	58988	0.9
NICER	3020560106	58989	0.6
NICER	3020560107	58991	5.2
NICER	3020560108	58992	3.2
NICER	3020560109	58994	0.8
NICER	3020560110	58997	1.7
NICER	3020560111	58998	1.0
NICER	3020560112	58999	1.3
NICER	3020560113	59000	1.1
NICER	3020560114	59001	2.7
NICER	3020560115	59002	1.0
NICER	3020560116	59003	0.7
NICER	3020560117	59004	1.4
NICER	3020560118	59005	1.2
NICER	3020560119	59006	1.0
NICER	3655010301	59017	1.2
NICER	3655010302	59018	6.6
NICER	3655010303	59018	4.1
NICER	3020560120	59020	0.9
NICER	3020560121	59021	0.8

Table A1
(Continued)

Telescope	ObsID	MJD	Exposure ks
NICER	3020560122	59022	1.7
NICER	3020560123	59023	3.2
NICER	3020560124	59024	1.8
NICER	3020560125	59025	1.7
NICER	3020560126	59027	0.8
NICER	3020560127	59028	1.7
NICER	3020560128	59029	1.7
NICER	3020560129	59030	2.2
NICER	3020560130	59031	0.6
NICER	3020560131	59032	1.2
NICER	3020560132	59033	1.1
NICER	3020560133	59034	0.8
NICER	3020560134	59038	0.5
NICER	3020560135	59040	0.4
NICER	3020560136	59041	1.3
NICER	3020560137	59042	0.7
NICER	3020560138	59045	3.1
NICER	3020560139	59046	1.4
NICER	3020560140	59047	0.9
NICER	3020560141	59049	0.8
NICER	3020560142	59056	0.2
NICER	3020560143	59061	1.3
NICER	3020560144	59062	1.4
NICER	3020560145	59063	0.5
NICER	3020560146	59064	2.0
NICER	3020560147	59065	0.8
NICER	3020560148	59067	2.2
NICER	3020560149	59089	0.3
NICER	3020560150	59102	0.1
NICER	3020560151	59103	2.1
NICER	3020560152	59111	1.2
NICER	3020560153	59117	1.5
NICER	3655010401	59128	9.1
NICER	3655010402	59129	14.5
NICER	3020560154	59131	0.9
NICER	3020560155	59132	1.9
NICER	3020560156	59133	0.3
NICER	3020560157	59135	2.1
NICER	3020560158	59135	0.7
NICER	3020560159	59138	1.3
NICER	3020560160	59139	11.1
NICER	3020560161	59140	5.8
NICER	3020560162	59141	13.5
NICER	3020560163	59141	16.8
NICER	3020560164	59143	6.6
NICER	3020560165	59143	4.4
NICER	3020560166	59146	7.4
NICER	3020560167	59147	6.0
NICER	3020560168	59147	8.4
NICER	3020560169	59150	2.3
NICER	3020560170	59165	2.6
NICER	3020560171	59166	6.7
NICER	3020560172	59172	4.4
NICER	5020560106	59864	1.3
NICER	5020560107	59865	14.9
NICER	5020560108	59875	0.3
NICER	5020560109	59877	0.7
NICER	5020560110	59888	1.2

Table A1
(Continued)

Telescope	ObsID	MJD	Exposure ks
NICER	5020560111	59889	0.7
NICER	5020560112	59892	1.2
NICER	5020560113	59893	1.7
NICER	5020560114	59894	8.3
NICER	5020560115	59895	10.8
NICER	5020560116	59896	7.1
NICER	5020560117	59897	11.0
NICER	5020560118	59902	0.4
NICER	5020560121	59923	0.7
NICER	5020560122	59924	0.8
NICER	5020560123	59929	1.0
NICER	5020560124	59932	2.5
NICER	5020560125	59933	1.5
NICER	5576010101	59865	3.1
NICER	5576010102	59866	10.0
NICER	5576010103	59867	7.8
NICER	5576010104	59869	10.0
NICER	5576010105	59870	2.6
NICER	5576010106	59871	2.5
NICER	5576010107	59872	2.7
NICER	5576010108	59873	1.7
NICER	5576010109	59874	3.0
NICER	5576010110	59875	2.0
NICER	5576010111	59878	6.6
NICER	5576010112	59886	0.8
NICER	5576010113	59889	1.1
NICER	5576010114	59893	1.1
NICER	5576010115	59895	0.4
NICER	5576010116	59898	0.8
NICER	5576010117	59901	1.2
NICER	5576010121	59913	0.9
NICER	5576010122	59925	2.1

Note. The time resolutions of Chandra observations 15874, 15875, 17314, and 18884 are 0.44 s, 2.85 ms, 2.85 ms, and 2.85 ms, and those of XMM-Newton and NICER are 68.7 ms and 1 μ s, respectively.

References

- Archibald, R. F., Kaspi, V. M., Ng, C. Y., et al. 2013, *Natur*, **497**, 591
Archibald, R. F., Kaspi, V. M., Scholz, P., et al. 2017, *ApJ*, **834**, 163
Archibald, R. F., Kaspi, V. M., Tendulkar, S. P., & Scholz, P. 2016, *ApJL*, **829**, L21
Archibald, R. F., Scholz, P., Kaspi, V. M., Tendulkar, S. P., & Beardmore, A. P. 2020, *ApJ*, **889**, 160
Bachetti, M., Markwardt, C. B., Grefenstette, B. W., et al. 2021, *ApJ*, **908**, 184
Baym, G., & Pines, D. 1971, *AnPhy*, **66**, 816
Bochenek, C. D., Ravi, V., Belov, K. V., et al. 2020, *Natur*, **587**, 59
Borghese, A., Coti Zelati, F., Israel, G. L., et al. 2022, *MNRAS*, **516**, 602
Borghese, A., Coti Zelati, F., Rea, N., et al. 2020, *ApJL*, **902**, L2
Cai, C., Xue, W.-C., Li, C.-K., et al. 2022, *ApJS*, **260**, 24
CHIME/FRB Collaboration, Andersen, B. C., Bandura, K. M., et al. 2020, *Natur*, **587**, 54
Dai, S., Johnston, S., Weltevrede, P., et al. 2018, *MNRAS*, **480**, 3584
Dai, Z. G. 2020, *ApJL*, **897**, L40
Dib, R., & Kaspi, V. M. 2014, *ApJ*, **784**, 37
Dib, R., Kaspi, V. M., & Gavril, F. P. 2009, *ApJ*, **702**, 614
Dong, F. A. & Chime/Frb Collaboration 2022, *ATel*, **15681**, 1

- Enoto, T., Hu, C.-P., Guver, T., et al. 2022, *ATel*, **15690**, 1
- Ferdman, R. D., Archibald, R. F., & Kaspi, V. M. 2015, *ApJ*, **812**, 95
- Frederiks, D., Ridnaia, A., Svinkin, D., et al. 2022, *ATel*, **15686**, 1
- Gavriil, F. P., Dib, R., & Kaspi, V. M. 2011, *ApJ*, **736**, 138
- Ge, M. Y., Lu, F. J., Qu, J. L., et al. 2012, *ApJS*, **199**, 32
- Ge, M. Y., Lu, F. J., Yan, L. L., et al. 2019, *NatAs*, **3**, 1122
- Ge, M. Y., Zhang, S. N., Lu, F. J., et al. 2020, *ApJ*, **896**, 55
- Gendreau, K. C., Arzoumanian, Z., Adkins, P. W., et al. 2016, *Proc. SPIE*, **9905**, 99051H
- Geng, J., Li, B., & Huang, Y. 2021, *Innov*, **2**, 100152
- Harrison, F. A., Craig, W. W., Christensen, F. E., et al. 2013, *ApJ*, **770**, 103
- Hobbs, G. B., Edwards, R. T., & Manchester, R. N. 2006, *MNRAS*, **369**, 655
- Huang, Y. X., Xu, H., Xu, Y. H., et al. 2022, *ATel*, **15707**, 1
- Huang, Z.-P., Yan, Z., Shen, Z.-Q., et al. 2021, *MNRAS*, **505**, 1311
- Içdem, B., Baykal, A., & Inam, S. Ç. 2012, *MNRAS*, **419**, 3109
- Israel, G. L., Esposito, P., Rea, N., et al. 2016, *MNRAS*, **457**, 3448
- Jansen, F., Lumb, D., Altieri, B., et al. 2001, *A&A*, **365**, L1
- Kaneko, Y., Göğüş, E., Baring, M. G., et al. 2021, *ApJL*, **916**, L7
- Kirsten, F., Snelders, M. P., Jenkins, M., et al. 2021, *NatAs*, **5**, 414
- Kozlova, A. V., Israel, G. L., Svinkin, D. S., et al. 2016, *MNRAS*, **460**, 2008
- Kumar, P., & Bošnjak, Ž. 2020, *MNRAS*, **494**, 2385
- Li, C., Cai, C., Xiong, S., et al. 2022, *ATel*, **15698**, 1
- Li, C. K., Lin, L., Xiong, S. L., et al. 2021, *NatAs*, **5**, 378
- Li, Q.-C., Yang, Y.-P., Wang, F. Y., Xu, K., & Dai, Z.-G. 2022, *MNRAS*, **517**, 4612
- Li, X., Zhang, S., Xiong, S., et al. 2022, *ATel*, **15708**, 1
- Lin, L., Göğüş, E., Roberts, O. J., et al. 2020a, *ApJL*, **902**, L43
- Lin, L., Göğüş, E., Roberts, O. J., et al. 2020b, *ApJ*, **893**, 156
- Link, B., Epstein, R. I., & Baym, G. 1992, *ApJL*, **390**, L21
- Livingstone, M. A., Kaspi, V. M., & Gavriil, F. P. 2010, *ApJ*, **710**, 1710
- Lower, M. E., Younes, G., Scholz, P., et al. 2023, *ApJ*, **945**, 153
- Lu, W., Kumar, P., & Zhang, B. 2020, *MNRAS*, **498**, 1397
- Lyne, A. G., Smith, F. G., & Pritchard, R. S. 1992, *Natur*, **359**, 706
- Lyubarsky, Y. 2020, *ApJ*, **897**, 1
- Maan, Y., Leeuwen, J. v., Straal, S., & Pastor-Marazuela, I. 2022, *ATel*, **15697**, 1
- Mereghetti, S., Savchenko, V., Ferrigno, C., et al. 2020, *ApJL*, **898**, L29
- Metzger, B. D., Margalit, B., & Sironi, L. 2019, *MNRAS*, **485**, 4091
- Palfreyman, J., Dickey, J. M., Hotan, A., Ellingsen, S., & van Straten, W. 2018, *Natur*, **556**, 219
- Palm, D. M. 2022, *ATel*, **15667**, 1
- Perna, R., & Pons, J. A. 2011, *ApJL*, **727**, L51
- Ridnaia, A., Svinkin, D., Frederiks, D., et al. 2021, *NatAs*, **5**, 372
- Roberts, O., Dalessi, S., & Malacaria, C. 2022, *ATel*, **15672**, 1
- Ruderman, M., Zhu, T., & Chen, K. 1998, *ApJ*, **492**, 267
- Şaşmaz Muş, S., Aydın, B., & Göğüş, E. 2014, *MNRAS*, **440**, 2916
- Shaw, B., Keith, M. J., Lyne, A. G., et al. 2021, *MNRAS*, **505**, L6
- Shen, J.-Y., Zou, Y.-C., Yang, S.-H., Zheng, X.-P., & Wang, K. 2023, *ApJ*, **951**, 3
- Tavani, M., Casentini, C., Ursi, A., et al. 2021, *NatAs*, **5**, 401
- Thompson, C., & Duncan, R. C. 1995, *MNRAS*, **275**, 255
- Tong, H. 2023, *RAA*, **23**, 025013
- Wadiasingh, Z., Beniamini, P., Timokhin, A., et al. 2020, *ApJ*, **891**, 82
- Wang, C., Xiong, S., Zhang, Y., et al. 2022, *ATel*, **15682**, 1
- Wang, P., Li, J., Ji, L., et al. 2023, *arXiv:2308.08832*
- Wang, W.-H., Xu, H., Wang, W.-Y., et al. 2021, *MNRAS*, **507**, 2208
- Woods, P. M., Kaspi, V. M., Thompson, C., et al. 2004, *ApJ*, **605**, 378
- Woods, P. M., Kouveliotou, C., van Paradijs, J., et al. 1999, *ApJL*, **524**, L55
- Wu, Q., Zhao, Z.-Y., & Wang, F.-Y. 2023, *MNRAS*, **523**, 2732
- Yang, Y.-P., & Zhang, B. 2018, *ApJ*, **868**, 31
- Yang, Y.-P., & Zhang, B. 2021, *ApJ*, **919**, 89
- Younes, G., Baring, M. G., Harding, A. K., et al. 2023, *NatAs*, **7**, 339
- Younes, G., Burns, E., Roberts, O., et al. 2022, *ATel*, **15794**, 1
- Younes, G., Kouveliotou, C., Jaodand, A., et al. 2017, *ApJ*, **847**, 85
- Younes, G., Ray, P. S., Baring, M. G., et al. 2020a, *ApJL*, **896**, L42
- Younes, G., Güver, T., Kouveliotou, C., et al. 2020b, *ApJL*, **904**, L21
- Yuan, Y., Beloborodov, A. M., Chen, A. Y., & Levin, Y. 2020, *ApJL*, **900**, L21
- Zhang, B. 2017, *ApJL*, **836**, L32
- Zhang, B. 2020, *ApJL*, **890**, L24
- Zhang, C. F., Jiang, J. C., Men, Y. P., et al. 2020, *ATel*, **13699**, 1
- Zhang, Y. H., Ge, M. Y., Lu, F. J., et al. 2022, *ApJ*, **932**, 11
- Zhu, W., Xu, H., Zhou, D., et al. 2023, *SciA*, **9**, ead6198